Calculations for, and laboratory measurements of a multistage labyrinthine baffle for "SMEI"

Andrew Buffington[*], Bernard V. Jackson**, and Paul P. Hick***
Center for Astrophysics and Space Sciences, University of California, San Diego

ABSTRACT

The spaceborne Solar Mass Ejection Imager (SMEI) is scheduled for launch into near-earth orbit (>800 km) in early 2003. Three SMEI CCD cameras on the zenith-oriented CORIOLIS spacecraft cover most of the sky each 100-minute orbit. Data from this instrument will provide precision visible-light photometric maps. Once starlight and other constant or slowly varying backgrounds are subtracted, the residue is mostly sunlight that has Thomson-scattered from heliospheric electrons. These maps will enable 3-dimensional tomographic reconstruction of heliospheric density and velocity. The SMEI design provides three cameras, one of which views to within 18 degrees of the solar disk with a field of view 60° long by 3° wide. Placed end-to-end, three fields of view then cover a nearly 180° long strip that sweeps out the sky over each orbit. The 3-dimensional tomographic analysis requires 0.1% photometry and background-light reduction below one S10 (the brightness equivalent of a 10th magnitude star per square degree). Thus 10^{-15} of surface-brightness reduction is required relative to the solar disk. The SMEI labyrinthine baffle provides roughly 10^{-10} of this reduction; the subsequent optics provides the remainder. We describe the baffle design and present laboratory measurements of prototypes that confirm performance at this level.

Keywords: Background-light reduction; space optics; very wide-angle optical designs

1. INTRODUCTION

Data from the two HELIOS spacecraft[1] show that solar mass ejections can be viewed in Thomson-scattered visible light and followed from the Sun's outer corona to 1AU and beyond[2-5]. The "Solar Mass Ejection Imager" (SMEI)[6-12] is a logical descendent of this HELIOS heritage. SMEI will cover nearly the entire sky in visible light, each near-Earth 100-minute orbit, and is designed to map large-scale variations in heliospheric electron densities. It will provide roughly 10-fold improved angular and photometric resolution compared with HELIOS, and a fivefold faster cadence for full-sky maps. In addition to providing up to three days advance warning of solar mass ejection arrivals at Earth, SMEI will resolve and track their evolution to well beyond 1 AU. In addition, it will image co-rotating structures[13], coronal streamers, density enhancements behind interplanetary shock waves, comets, and comet bow shocks[14]; it will map irregularities in the zodiacal dust-cloud distribution; and it will search for near-Earth objects[15].

SMEI uses three separate CCD cameras viewing away from Earth to cover most of the sky during each orbit. Each camera views a $60° \times 3°$ field of view (FOV) of the sky with a 2×1 cm aperture and 4 sec exposures. The images are frame-transferred and read out during the period of the next exposure. Each camera aperture is protected by a stray-light-reducing baffle, whose design and calibration are the main focus of this article. The three cameras are aligned to view a $180° \times 3°$ strip oriented perpendicular to the satellite's velocity vector. SMEI is designed to look within 18° of the Sun's limb in the narrow dimension of its FOV. The 4 sec exposure time guarantees that a given place in the sky will be covered by at least 12 frames each orbit, except for an excluded zone near the Sun, another with the Moon near the FOV, and small regions near the four brightest planets. SMEI is presently scheduled for an early 2003 launch date. The satellite to be employed, "CORIOLIS", is part of the Air Force's Space Test Program and has a sun-synchronous, near-polar terminator orbit at $\gtrsim$800 km altitude. SMEI was designed and constructed by a team of scientists and engineers from the U. S. Air Force Research Laboratory, UCSD, the University of Birmingham UK, Boston College, and Boston University. Financial support is being provided by the Air Force, the University of Birmingham and NASA.

SMEI will forecast solar mass ejections heading toward Earth. Individual camera frames over an orbit will be combined into a "heliospheric sky map" from which the unchanging stellar and zodiacal backgrounds can be removed.

Innovative Telescopes and Instrumentation for Solar Astrophysics, Stephen L. Keil, Sergey V. Avakyan, Editors, Proceedings of SPIE Vol. 4853 (2003) © 2003 SPIE · 0227-786X/03/$15.00

Recognizable features, moving from one map to the next, directly provide a measure of angular velocity, which determines two out of three velocity components provided an estimate of the distance is available. More powerful analysis is required to fully quantify mass and velocity. Changing sky brightnesses measured from SMEI enable tomographic reconstruction, determining the shapes of heliospheric structures in 3 dimensions by assuming a radially expanding solar wind. These tomographic techniques have successfully mapped co-rotating heliospheric structures using both interplanetary scintillation[16-18] and Thomson-scattering observations from the HELIOS photometers[19,20]. More recently, "time-dependent" tomographic analyses have reconstructed 3-dimensional heliospheric structures from outward plasma flow alone[21] and have modeled the arrival at Earth of both corotating structures and coronal mass ejections (CMEs)[22]. The improved quality of SMEI observations will greatly enhance this application of tomography to rapidly evolving structures such as CMEs.

When observations are also available from similar other imagers deployed to deep space, true stereoscopic imaging becomes possible, which eases the above assumption of purely radial expansion. When combined with solar observations of flare brightenings, disappearing filaments, coronal-hole locations, magnetic fields, and additional heliospheric observations such as velocity interplanetary scintillation measurements, the forecast capability of SMEI improves considerably.

2. SIGNAL LEVELS

A slowly rotating low-Earth orbiter with significant light in each pixel allows a CCD detector to integrate the incoming photons. This permits the signal to build up well above the CCD's statistical-noise readout level. Consider first the brightness range of objects within the FOV. The Thomson-scattered coronal light must be detected in the presence of diffuse background from many sources: light scattered into the FOV from bright sources such as the Sun, Moon, or Earth; the zodiacal light; and stars, individually as bright point sources or collectively as a contribution to diffuse sky brightness. Figure 1 shows the surface brightness of starlight and the zodiacal cloud as a function of heliospheric elongation ε. Starlight varies by a factor of three above and below the "stars" solid line in figure 1, depending on galactic coordinates. The brightest sky is closest to the Sun; with SMEI's coverage of $\sim 20° < \varepsilon < 180°$, brightness ranges over about a factor of 50. Figure 1 also shows expected CME brightnesses. **Solar mass ejections are typically only about 1% of the ecliptic zodiacal light.** Thus, to study these, the effective dynamic range of the instrument must be at least 4 decades.

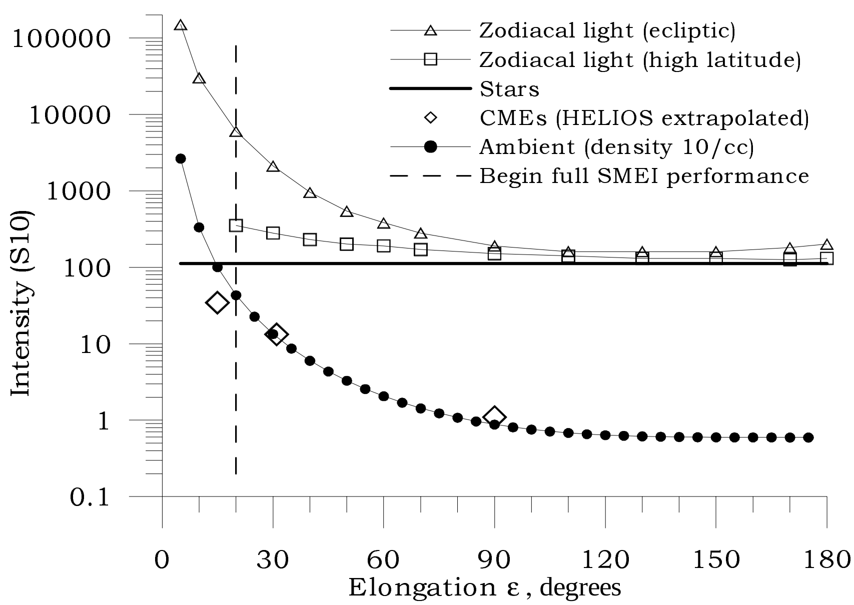

Figure 1. Surface brightness versus solar elongation, for zodiacal and star light, data taken from Astrophysical Quantities[23], and of expected coronal mass ejection (CME) brightnesses extrapolated from HELIOS measurements. A calculation of the brightness of an ambient medium having a density of 10 electrons/cm^3 at 1 AU and a spherically-symmetric inverse-square density dropoff with distance from the Sun is shown for comparison. An S10 unit is the equivalent brightness of a 10th magnitude star in a square degree.

The angular resolution is determined by the smallest sky bin in which heliospheric signals can be detected (at a 1-σ level) above the far brighter star- and zodiacal-light background. This occurs when the signal exceeds the noise for this bin. The SMEI aperture is sized for known sources of noise to deliver a 1-σ threshold of about 0.3 S10 units, averaged over a single orbit with $1° \times 1°$ sky bins. Thus SMEI offers a 3-σ threshold of about one S10 unit per bin, good enough to detect new heliospheric features occupying only a few bins at 90° elongation. About ¼ of this error budget is due to the counting-statistics shot noise. Most of the remainder comes from subpixel-response-gradient noise in the photometry[24,25], and from error caused by uncertainty in combining individual frames into a heliospheric sky map. The particular EEV CCD chip chosen has in laboratory tests delivered the desired 0.1% differential photometry for SMEI images. The Sun's brightness at 1 AU is about –26 magnitudes, nearly 10^{15} times that of a typical CME at $\varepsilon = 90°$. Thus the combination of baffle plus optics for SMEI must reduce scattered sunlight by a factor of about 10^{-15} for quantitative measurements and 3-dimensional CME reconstructions.

Zodiacal light, the Milky Way, and other starlight are generally brighter than the desired variable Thomson-scattered signal, and for 3-dimensional reconstruction must be removed from the data. HELIOS found that zodiacal light is unchanging in time and spatially smooth, to near the desired detection brightness threshold for SMEI. Knowing the sky orientation of each data frame permits removal of this background light, by using either an empirical model or an average from previous orbits. Stars are dealt with in a similar fashion. However, because stars are unresolved and highly structured spatially on the sky maps, the location and orientation of each sky resolution element must be known to high precision to enable an effective background subtraction.

3. BAFFLE-DESIGN BACKGROUND

CORIOLIS will be in a sun-synchronous terminator orbit. Since each SMEI camera views a large angle in only one dimension, a slit-type baffle is employed. The brightest objects contributing background light are the Sun, Earth, and Moon. From low-Earth orbit the Earth is almost as bright as the Sun and covers nearly half a celestial sphere. SMEI controls background light first by pointing its cameras away from the Earth, and then by (usually) keeping the Sun more than 20° from the FOV of the nearest-Sun-facing camera. The baffle design itself controls the remaining scattered light from the Earth and Sun.

Stray-light control here employs a labyrinthine array of multiple apertures and septa to restrict stray-light access to the main optical system aperture[26,27]. The baffle surfaces are suitably blackened to dispose of, rather than scatter, most of the stray light. Such surfaces typically reflect 1% or less of the incident light, and re-radiate the residue isotropically (a Lambertian distribution)[28-30]. Further, when one or more outer sections of the labyrinth are brightly illuminated, light scattered from the aperture edges diffracts over subsequent apertures and some of this finds its way through the baffle[31]. Of the overall SMEI specification, namely a 10^{-15} total stray-light surface-brightness reduction in the FOV relative to the Sun, the baffle provides 10^{-10}, and the subsequent optics an additional 10^{-5}. Such stringent rejection factors are difficult to achieve, even with much smaller FOVs[31], and reaching this goal has received close attention from the very beginning of SMEI design. The baffle employs 9 rectangular apertures including the optical pupil. We distinguish here between *principal* and *secondary* apertures[†], where the former define the entrance and exit planes of the "baffle stages", and the latter are placed within stages to block light that would otherwise have a single-scattering path off the bottom of the septum structure connecting these planes. The next section describes an analytic method for optimally locating and sizing a secondary aperture.

4. A SIMPLE SINGLE-STAGE BAFFLE

Consider two parallel planes separated by distance d and having square aperture holes with openings of half-size respectively x_1 and x_2, centered on a normal to the planes. Illuminate aperture #1 with surface brightness I_0 at angle θ relative to the normal. Assume the remainder of the planes each has reflectivity $R << 1$ and that θ is large enough that no incident light directly illuminates aperture #2. Finally, assume that negligible light diffracts past aperture #1 and then passes through aperture #2. In this case, light that *does* find its way through aperture #2 is dominated by a first scattering

[†] Note that the present concept "apertures" is elsewhere in the literature called also "baffles", "vanes", or "glare stops"[26,31].

from plane #2, a re-scattering from plane #1, and the angles such that the twice-scattered light then passes through aperture #2. Total transmitted light I_t is thus given by:

$$I_t \approx I_0 \ (2x_1)^2 \ \cos\theta \ \ R^2 \ \ \Omega_1 \Omega_2 / (2\pi)^2 \qquad , \tag{1}$$

including incident light, projected area ($\cos\,\theta$ obliquity), and finally for each scattering both an R and a geometrical factor (steradians). To make eq (1) exact, the $\Omega_1\Omega_2$ term should be a double integral over angular domains of both scatterings, convolved with a step function to represent the double scattering successfully passing through aperture #2. Eq (1) approximates these as separable average factors. Carrying this approximation further:

$$\Omega_1 \approx \cos^2\theta \ , \qquad \Omega_2 \approx (2x_2)^2 / d^2 \qquad , \tag{2}$$

where Ω_1 represents the probability that the first scattering of a particular ray returns it to a place on the back surface of aperture #1 relatively near to its opening, and Ω_2 is the average solid angle of aperture #2 as viewed from that place. Combining eqs (1) and (2):

$$I_t \approx (4/\pi^2) \ \ I_0 \ \ (x_1 x_2 / d)^2 \cos^3\theta \ \ R^2 \qquad . \tag{3}$$

Here the R^2 term represents the presence of two scatterings; and $\cos^3\,\theta$ represents the original obliquity plus two more powers for the diminishing solid angle subtended by the first scattering, for light to head back near aperture #1, where the second scattering has a decent chance of reaching aperture #2.

Practical size and mounting limitations usually dictate a finite transverse extent to the aperture structures rather than the above infinite planes. Aperture planes are now attached to one another by a septum, whose bottom interferes with the validity of eqs (1→3) by introducing paths whereby some light can, with only one scattering, pass through the second aperture, when θ is large enough that the septum bottom is illuminated. The double-scattering criterion can be restored by the addition of a secondary aperture, provided the septum is not too shallow. Figure 2 shows a typical single-stage baffle.

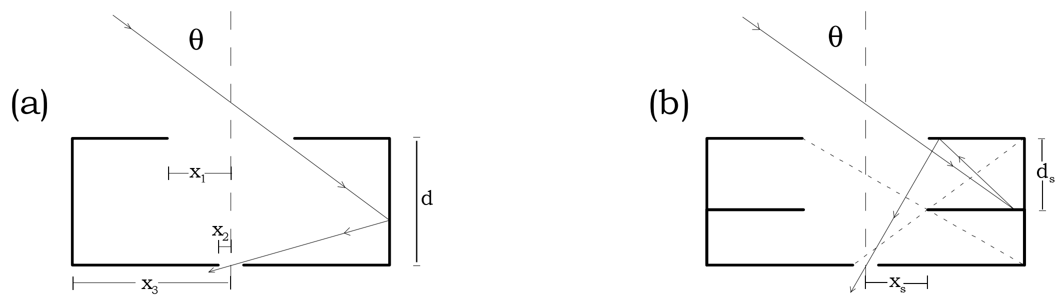

Figure 2. Two simple baffles, one without and one with a secondary aperture, which illustrate control of the single-scattering-from-a-septum path. (a) Two primary apertures and a septum: a light ray incident at a wide angle θ through aperture #1 at the top, scatters once from the septum (right) and then passes through aperture #2 at the bottom. (b) Addition of a secondary aperture, whose size of opening x_s and vertical position d_s is defined by the intersection of the two finely dashed lines. This secondary aperture completely blocks aperture #2 from viewing the septum above, and aperture #1 from illuminating the septum below, thus restoring the requirement of a double scattering, for wide-angle light to reach aperture #2 from aperture #1.

The opening size x_s and displacement d_s of this secondary aperture are given by

$$x_s = \frac{x_3^2 - x_1 x_2}{x_1 + x_2 + 2x_3} \quad , \qquad d_s = d\,\frac{x_1^2 + 2x_1 x_3 + x_3^2}{(x_1 + x_3)(x_1 + x_2 + 2x_3)} \qquad . \tag{4}$$

The requirement that this aperture *be* truly secondary, *i.e.* not protrude into the pyramidal volume defined by apertures # 1 and 2, becomes

$$x_s > x_1 - (x_1 - x_2)\, d_s / d \quad . \tag{5}$$

When eq (5) is not satisfied, single-scattering paths may yet be avoided with more than one secondary aperture and/or a pyramidal septum.

Confirmation of eq (3) and the above secondary-aperture reasoning, for the case of the particular apertures and spacing illustrated in figure 2, is made by numerical calculations using the ray-tracing program "ZEMAX"[32]. Figure 3 shows the results. These calculations also show that two scatterings effectively smear the light passing through aperture #2 over a wide range of angles, although most of this light *is* headed away from the particular region directly illuminated by the incident light. Thus, when combining several stages to make a complete baffle design, the average wide-angle light rejection for second and further stages can simply multiply the first-stage graph, the analog of figure 3 for a given design.

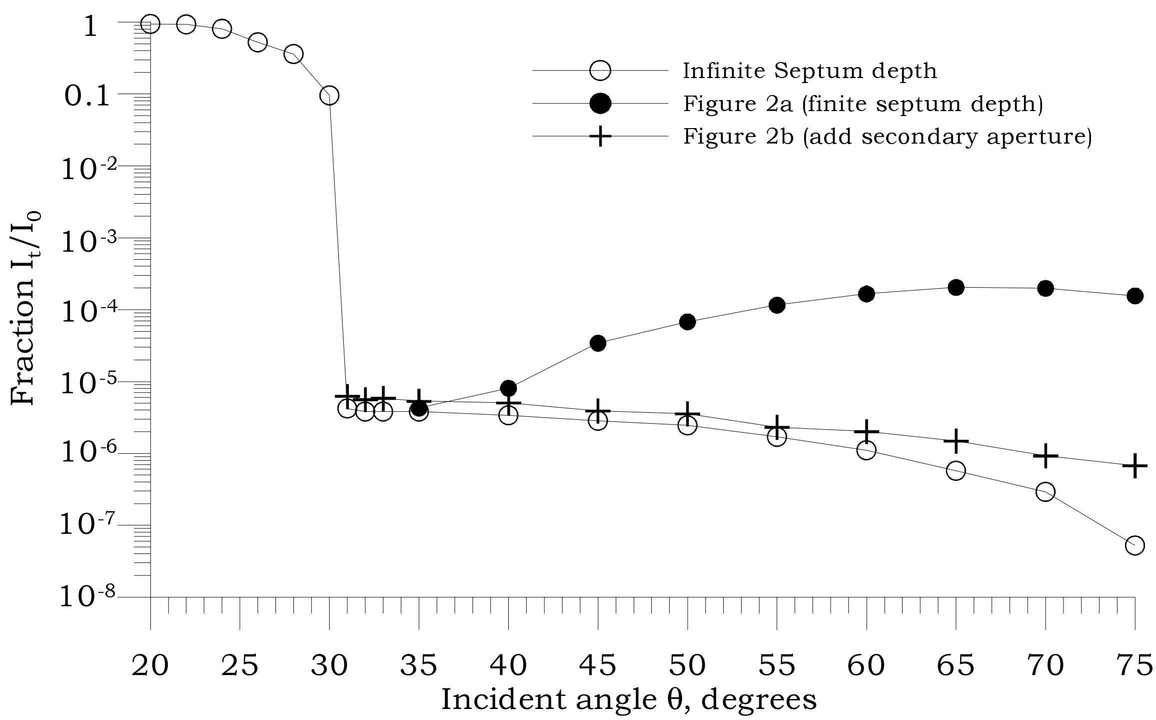

Figure 3. Fractional light transmission versus angle for the single-stage baffle geometry illustrated in figure 2, with $R = 0.01$ and normalized to unity at $\theta = 0°$. Overlap between the two apertures drops to zero as $20° < \theta < 30°$. Above this, eq (3) is valid for the infinite septum case (open circles), and I_t/I_0 plummets due to the R^2 term; at larger angles the $\cos^3 \theta$ term causes a further slow dropoff. For finite septum depth (closed circles), eq (3) holds until $\theta > 36°$ when the septum bottom is illuminated and a single-scattering path opens up. Starting here, performance degrades with increasing θ, due to the loss of a factor $R \cos^2 \theta$. Performance is almost restored with the addition of a secondary aperture (crosses), but not quite, due to the loss of a $\cos^2 \theta$ term in Ω_1 and increased Ω_2 from shorter scattering paths.

5. SMEI APERTURE PLACEMENT

Primary apertures in a baffle configuration are positioned such that each successively masks the light from entering the aperture opening in the plane below it[26,27]. The present SMEI design began with an evaluation prototype for the WIND spacecraft[6]. This had a 1.27 × 1.27 cm rear opening, a 60° × 3° FOV and a Martin Black interior coating[28]. In its narrow dimension, a second stage cut off light at $\Theta_x > 22.5°$ from the baffle centerline, and a third stage at $\Theta_x > 60°$ provided more rejection[7]. Available spacecraft volume limited the design in the wide dimension to two stages, with the cutoff beginning at $\Theta_y > 60°$. This baffle's measured reduction for $\Theta_x > 22.5°$ was $\frac{1}{2} \times 10^{-7}$, about as expected. Its design calculations used the size of source and collector pairs (septum bottoms and apertures), the distances between them, the amount of incident light, and assumed reflectivity R, to determine the amount of light reduction at each reflection surface, similar to the method of section 3 above.

After this WIND-prototype performance confirmation, a brute-force parameter search evaluated 10^6 cases within the overall envelope, and found aperture positions optimized in the baffle's narrow dimension, a 2×1 cm final aperture, a second stage starting at $\Theta_x > 19.5°$, and a third at $\Theta_x > 54°$. At the edge of the FOV these reduced angles enabled looking as close as 18° to the Sun's limb and improved stray-light rejection. Aperture vanes were simply continued around in the baffle's wide dimension with both "stages" cutting in at $\Theta_y > 58°$.

To complete the SMEI baffle design, secondary apertures were added to block septum-bottom scattering paths (figure 4). Aperture Z2 was placed in both dimensions by the method described in section 3 above, but apertures Z4 and Z5 only in the narrow dimension; their vanes continued around in the wide dimension as for the primary apertures above. The remaining apertures, Z1 and Z7, only partially cover their respective septum bottoms and are thus not dominant contributors to the SMEI baffle performance. Only the innermost stage of the baffle achieves full performance in the sense of the previous section, by requiring double scattering as defined by eq (3). Each outer stage individually has *some* single-scattering paths, although the solid angle for these is significantly reduced by the secondary apertures and the slit design style. With light incident at a sufficiently large angle that *any* outer stage is operational, 3-scattering paths are sufficiently rare that the combined contribution from 4-scattering paths is not much smaller, even though the 3-scattering paths benefit from having one fewer factors of R.

Having 4-scattering paths with $R = 0.005$ insures overall flight-baffle performance near 10^{-10}, close to the desired SMEI specification, given the absence of other processes. However, the geometric scattering and solid-angle method above neglects diffraction over the aperture edges. When aperture-edges Z6, Z5, or Z4 are directly illuminated, a reduced (by R) intensity scatters off the edge, some of which heads towards Z0 and passes close to the edge of aperture Z3. A diffraction-deflection of only a few degrees for light originating from Z6 enables entry through Z0. In the SMEI design, the Z5 aperture size was enlarged a few millimeters over the value indicated by section 3, but its spacing (d_s) in the Z direction retained, to reduce its diffraction contribution and thus improve performance when $\Theta_x < 30°$ and the Z5 edge is illuminated. This compromise cost little in overall baffle performance because the portion of the septum bottom thus opened up to direct viewing through the Z3 aperture is always shadowed from direct illumination by its Z6 vane anyway. Figure 4 shows the SMEI baffle layout in both narrow and wide directions, Table 1 lists the aperture-opening sizes and spacings, and figure 5 is a photograph of the prototype baffle prior to application of the Martin Black interior surface. Aperture Z0 is rectangular for the present calculations, but is in reality a more complicated shape, similar to a racetrack having Table 1's length and width, and a corner radius of 0.425 cm.

Aperture (vane) number	aperture half-length X	aperture half-width Y	spacing relative to Z0
Z0	1.00	0.50	≡ 0.00
Z1	5.08	2.54	1.29
Z2	4.57	1.65	3.85
Z3	6.76	0.99	9.46
Z4	10.16	1.96	11.51
Z5	12.10	2.35	14.07
Z6	16.87	3.17	21.27
Z7	19.76	5.08	24.27
Z8	22.40	5.51	27.75

Table 1. Dimensions and spacings of the SMEI baffle apertures. X,Y are the wide and narrow dimensions and Z is along the baffle centerline. All apertures are rectangular. Units are centimeters.

The SMEI baffles are machined with a 30° bevel tapering down to a blunt edge 0.25 ± 0.05 mm in width. Applying Martin Black rounds this edge to a cylindrical shape approximately 0.1 mm in radius. The vane edges are sufficiently small that direct edge-to-edge scattering (as distinct from the diffraction just discussed) is negligible. Breault discusses the choice of orientation for the bevels on the vane structures[27]. The SMEI bevels all face towards Z0 except Z0 itself, whose bevel faces outward towards the incoming light.

We have previously presented a convenient graph for evaluating diffraction behind a single knife edge[33], derived from the treatment of Born and Wolf[34]. Here a dimensionless variable W describes the geometry of a particular calculation. Light diffracting over Z3 and passing through Z0, coming from respective Z6, Z5, and Z4 apertures in the narrow dimension, has W = 10, 40, and 70. The intensity reductions read from the graph (compared with what they would be in the absence of Z3) are respectively 5×10^{-4}, 3×10^{-5}, and 1×10^{-5}. Z0 subtends about 10^{-3} steradians from these. The illuminated area of a Z6 vane is about 0.25 cm^2, R = 0.005, and the resulting overall stray-light intensity I_t / I_0 is about 10^{-10} for Z6, and smaller $\propto$ W^{-2} for the others. Larger values of W in the wide dimension render diffraction over Z3's short side unimportant.

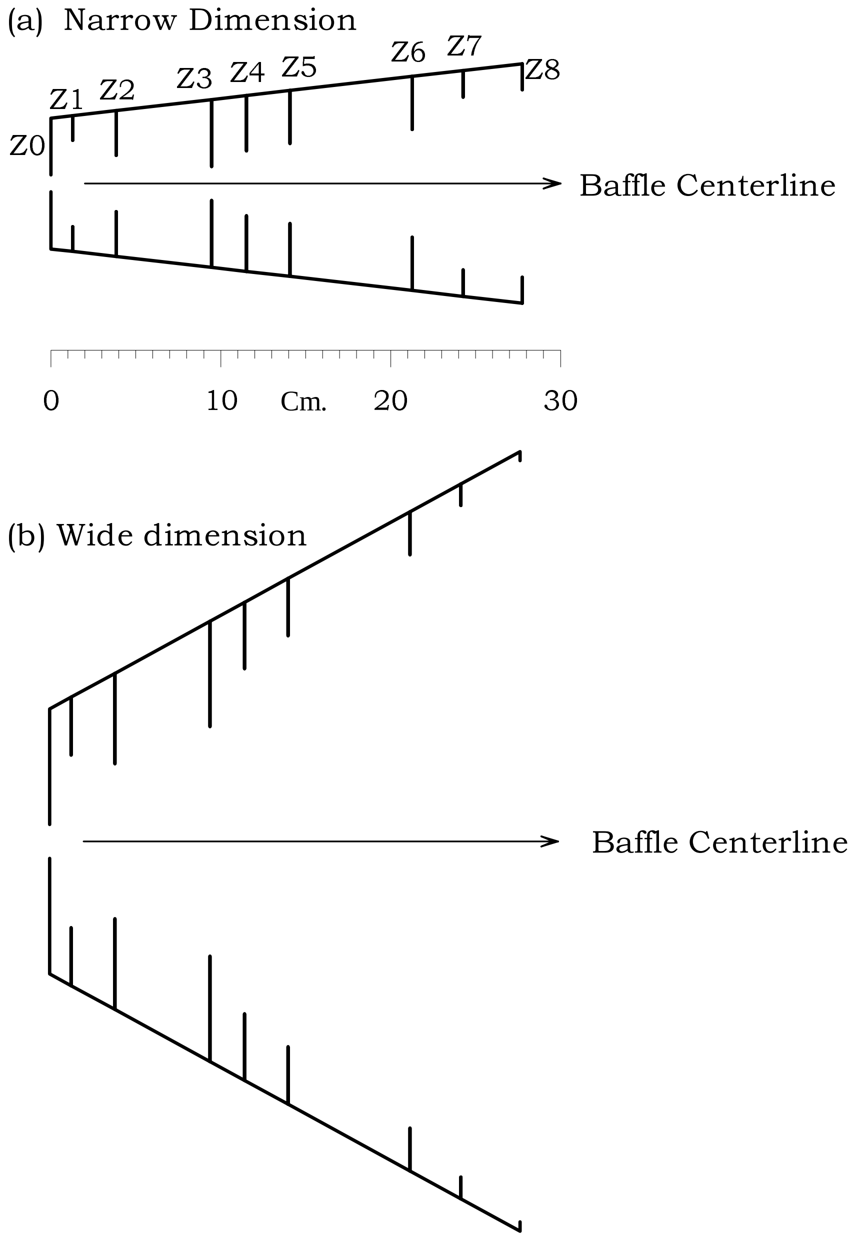

Figure 4. SMEI baffle design. Aperture numbers Z0 to Z8 advance with distance towards incident light along the baffle centerline. The strategic primary apertures are Z0 (rear of 1st stage and pupil of the subsequent SMEI optics, located out of sight off to the left here), Z3 (2nd stage rear), Z6 (3rd stage rear), and finally Z8 (3rd stage front). In the wide dimension the Z3, Z6 and Z8 edges line up, so here the "2nd stage" of the baffle extends from Z3 to Z8 and includes Z6. Secondary apertures Z4 → Z7 are placed between Z3 and Z8 to block illumination and/or viewing of the septum bottoms, as described in the text.

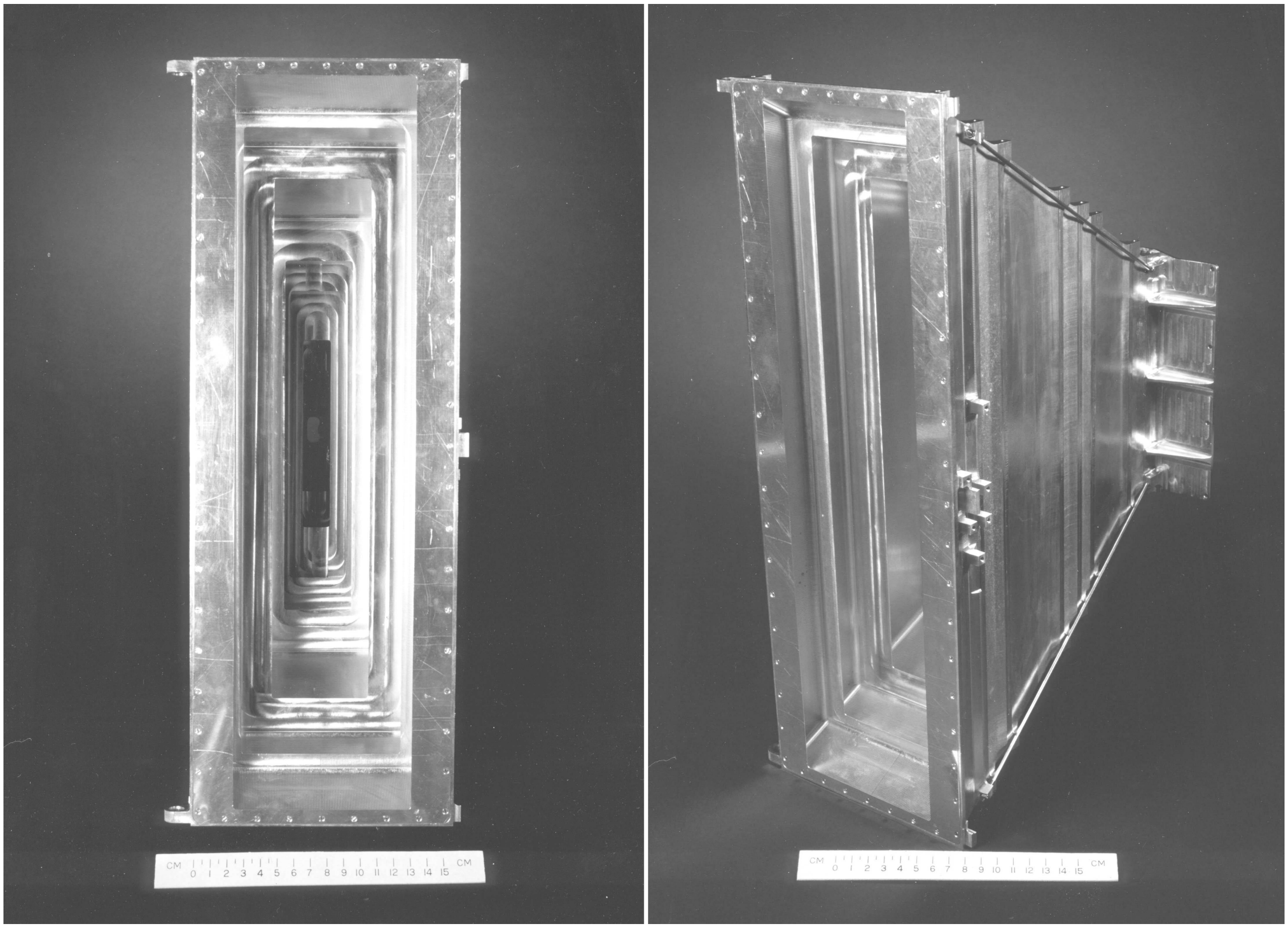

Figure 5. The SMEI prototype baffle, prior to application of the Martin Black surface. Left: front entrance, viewing along the optical axis/baffle centerline and showing the interior aperture structure. Right: oblique view showing front apertures and septum bottoms. The scale is 15 centimeters. This baffle, and the flight baffles were manufactured at the University of Birmingham, UK.

6. CALCULATIONS AND LABORATORY MEASUREMENTS

3.2 × 3.2 cm samples each received a Martin Black coating when a SMEI baffle was coated. Their reflectivity was measured at normal incidence by shining a laser beam onto the sample and viewing reflected light with a CCD camera. The apparent brightness of the reflected spot is then compared with the spot brightness when the sample is replaced by white paper. Measured reflectivity for the prototype baffle's Martin Black is about 0.01. The SMEI flight baffles have 0.005, in better agreement with the manufacturer's specification sheet[28].

The prototype above, after blackening, was mounted in a HEPA-filtered workstation in a darkened clean room at UCSD. Its field of view was mostly covered by two 100 × 120 cm black-velvet panels placed just outside the workstation, a distance of 142 cm from the front of the baffle. A CCD camera just behind the baffle looked through the Z0 aperture to view either 2 or 7 cm^2 of the Z3 rear depending on whether a 52 or 28 mm focal length camera lens was used. Subsequent SMEI optics reject stray light whose last scatter within the baffle is further than about 1 cm from the edge of the Z3 aperture hole. A 1 cm wide band around the hole in Z3 has 35 cm^2. Thus measured total diffuse light on the CCD was scaled by the ratio of areas (18× or 5×) to deduce relevant stray light passing through Z0 from Z3; this rear-band brightness was uniform on Z3 within a factor of two. This method excludes light reflected further out on Z3, or from Z2 or Z1. This wider-angle light is roughly ¾ of the total passing through Z0, unimportant for SMEI, but it *is* included in the full-baffle-performance calculations below.

Various portions of the prototype-baffle interior were illuminated by laser and the increase of surface brightness on Z3 measured. Total laser intensity was measured by directly shining the laser into the camera, with appropriate neutral-density filters to control saturation. The black-velvet wall disposed of light scattered back out the front of the baffle; its reflectivity was about 10^{-3}. We note in passing that another type of velvet suitable for space deployment has been developed[35], and we measure a small sample's reflectivity to be also about 10^{-3}. The clean room environment was vital for controlling the exposure of the baffle to dust during the measurements. It also reduced the number of CCD data frames (roughly a 100-fold reduction, down to 1 frame in 3) that were ruined by light scattering into the baffle from one or more large airborne dust particles that happened to be illuminated in the incident-light path. When this happened we simply took another picture.

The SMEI *flight* baffles were measured in a clean room at the University of Birmingham having a similar black-velvet wall to occupy the FOV. The procedure differed somewhat for these baffles because optics and CCDs were already attached, and do not normally view the rear of Z3. To remedy this, a 10° wedge prism was inserted just behind Z0; the choice of its four possible orientations determined which edge of Z3 would be in view within the FOV. The CCD chip was also displaced 4 to 5 mm further than normal from the optics to put the Z3 edge in focus. As with the UCSD measurements, the measured brightness was scaled by a suitable factor to include the whole illuminated Z3 area.

The laser was set to illuminate a spot several millimeters from the long edge of vane Z2. The light then scatters twice in order to pass through Z0. This case is similar to the situation in figure 2b, a single-stage baffle and secondary vane. Measured fractional rejection is about 10^{-8} for the prototype, roughly as expected from eq (1) when omitting the $(2x_1)^2$, so I_0 is total laser intensity, and using $R = 10^{-2}$, $\Omega_1 \approx 0.3$, and $\Omega_2 \approx 10^{-2}$. Rejection is ½ to ¼ of this for flight units, again as expected given their smaller *R*. This apparent fractional rejection must be multiplied by the ratio of Z3 to Z0 aperture areas (about 15×) to relate it to baffle performance when incident light fills the Z3 aperture.

The above measurement checks two-scattering performance in the first stage of the baffle when a laser beam is directly deposited on Z2. A similar check has illumination incident more realistically through the Z3 aperture. This was enabled by a 6 mm diameter paper disk (made of good-quality white bond using a hole punch) attached to a black thread. The disk and thread were manipulated through the baffle-front opening, carefully to avoid damaging the Martin Black surfaces, to deposit the disk at various locations on septum bottoms between Z5 and Z8, at the wide-dimension baffle ends. This disk increases the scattered light 40-fold when illuminated with the laser. The increased brightness enables the detection of a diffuse glow on the rear of Z3, but only when the illuminated disk has a direct view of the Z3 opening. Out of concern for the disk manipulation damaging the Martin Black surfaces, this measurement was omitted on the flight units. Measured fractional rejection here is about 4×10^{-10}, again about as expected, given the ~0.1 steradians solid angle subtended by the Z3 hole when viewed from typical paper-disk locations. Total rejection inferred for a three-scattering path here is 10^{-11}, when dividing by the 40-fold increase from the paper disk. The corresponding baffle-performance requires multiplying this by the ratio of the septum-bottom area illuminated at a given $[\Theta_x , \Theta_y]$ to the Z0 aperture area, a factor ranging from 0 to 60 depending on the incident angles.

A bright line appears on the edge of Z3 when the laser beam illuminates a spot on a long edge of vanes Z4, Z5, or Z6. This bright line's apparent length on Z3 is proportional to the CCD camera's aperture size, as expected for diffraction, while the length of a *real* scattering upon Z3 would be independent of this. For Z6, the amount of light detected is about 4×10^{-10} of the laser light. This is about as predicted, multiplying the {5×10^{-4} diffraction-intensity reduction for Z3 and Z6 (see the previous section just below table 1)} by $10^{-2} \times 10^{-3} \times 10^{-1}$, respectively factors of *R*, of solid angle for the light to scatter towards Z0, and finally the Z6 edge (0.1 mm wide) intercepting only a portion of the laser beam. Diffraction when illuminating Z5 or Z4 is respectively less by factors of 5 and 25, again roughly as expected. Diffraction measured with Z6 illuminated for the flight units was about ¼ that of the prototype. This is a bit better than expected given their reduced value of *R*. Since the equivalent area of a laser-beam-width × the length of a Z6 vane is comparable to the Z0 aperture area, flight baffle performance is about 1×10^{-10} when a long edge of Z6 is illuminated and light diffracts over Z3. Even though it seems to emanate from the edge of Z3, the diffracted light passing through Z0 is highly anisotropic. Its intensity is about tenfold reduced from the above, for the portion encountering the next SMEI optical element past Z0, and thus in effect is rendered comparable to the three-scattering performance discussed just above, even though the figures presented just below include diffraction at this higher level.

The prototype baffle was also checked using a 14 × 14 cm parallel white-light beam. This light source is not bright enough to produce a measurable diffuse illumination on the rear of Z3 unless $\Theta_x < 58°$ and $\Theta_y < 20°$, so some light passes directly through the Z3 aperture. Diffracted light, concentrated upon the edge of Z3, was observable at larger angles. Full-performance values were checked at three incident angles $[\Theta_x, \Theta_y]$ = [0°, 45°], 5×10^{-10}; [45°, 0°], 5.5×10^{-7}; and [70°, 0°], 4×10^{-10}; all these are in good agreement with the laser measurements.

Performance for this baffle design was originally evaluated using APART[36], and more recently calculated using ZEMAX[32]. As explained above, this article presents calculated full-baffle performance for *all* the light scattering through Z0, even though much of this is at wide angles and easily rejected by the subsequent optics. Figures 6 and 7 present results of the ZEMAX calculations, with R = 0.005.

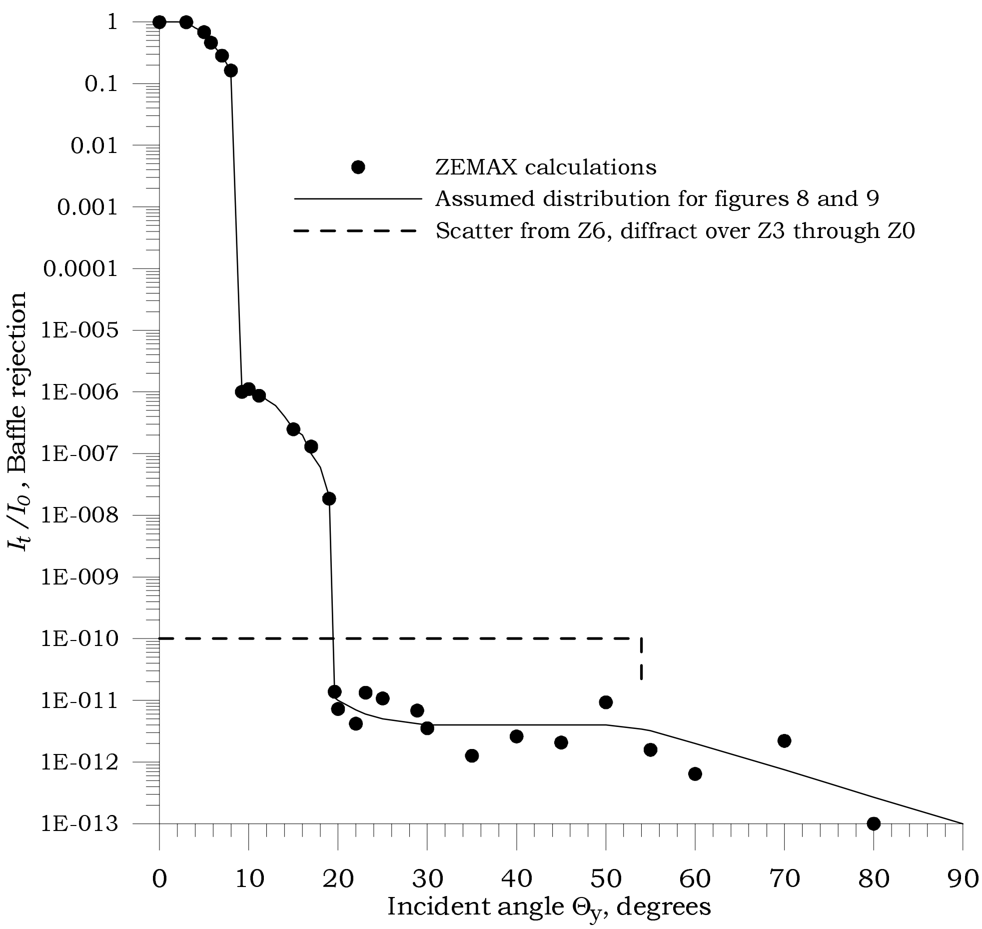

Figure 6. Stray-light rejection as a function of Θ_y, the incident-light direction across the FOV narrow dimension, for light incident at $\Theta_x = 0°$ calculated by ZEMAX. Fractional transmitted light is normalized to unity at 0°, as in figure 3. As Θ_y increases from 0°, I_t / I_0 drops off slowly at first, but then rapidly as the illuminated rectangle behind aperture Z3 overlaps less and less with the opening in Z0. At $\Theta_y \approx 9°$ the overlap disappears and a ray must scatter twice to pass through Z0. When $\Theta_y > 19.5°$ the overlap between Z3 and Z6 disappears and a third scattering is required, usually from a Z6, Z7 or Z8 septum bottom, see figure 4b. Light scattered from Z6 and diffracted over Z3 into Z0 is also shown here (dashed line); this dominates baffle rejection rather than multiple scattering, although not by a lot, for $\sim 20° < \Theta_y < 54°$. This plot and the next do not include the obliquity, here an extra factor of $\cos \Theta_y$. The smooth curve is used in generating figures 8 and 9. ZEMAX ray-tracing calculations include $1 \rightarrow 3 \times 10^7$ rays for $20° < \Theta_y < 54°$, and 10^8 rays for $\Theta_y > 54°$.

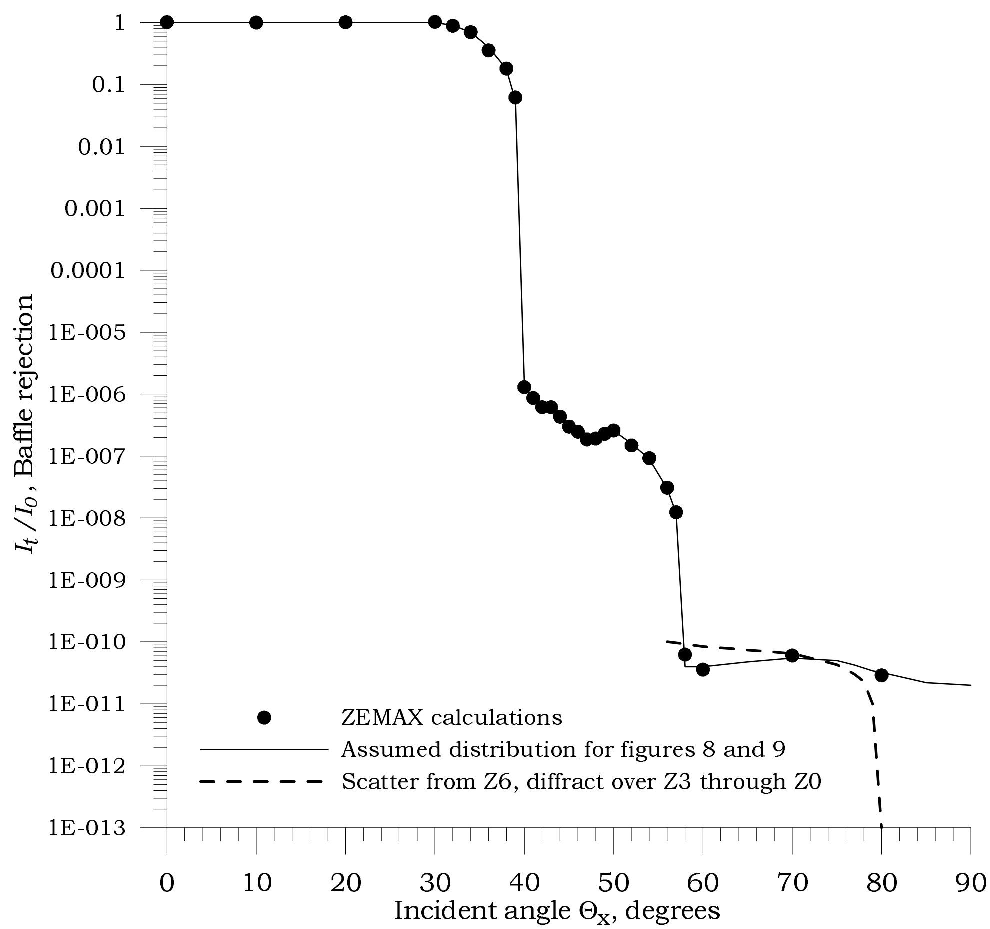

Figure 7. Similar to figure 6, but now exploring Θ_x, the wide dimension, with $\Theta_y = 0°$. Two-scattering paths dominate for $40° < \Theta_x < 58°$ and three-scattering paths above this. Diffraction over the Y-portion (the narrow dimension, see table 1 or figure 4b) of the Z3 aperture is negligible here, but diffraction over Z3 must be included for the X-portion of Z6 that is illuminated (dashed line).

7. CONCLUSIONS AND DISCUSSION

Figures 8 and 9 extend the results of figures 6 and 7 (incorporating the diffraction and including several extra ZEMAX calculations having both incident-light angles nonzero) to cover the whole range of $[\Theta_x,\Theta_y]$. An appropriate cos Θ_R obliquity factor is now included, where $\cos \Theta_R = \cos \Theta_x \times \cos \Theta_y$. We caution, however, that these results include *all* light passing through Z0, even though the laboratory measurements above include only light diffracted past Z3 or with a last scattering within the 1 cm wide band around the opening on the rear of Z3. Strictly, the overall SMEI stray-light rejection includes also the further light rejection of the subsequent optics, which *is* especially effective at eliminating the wider-angle light passing through Z0.

SMEI will be capable of tracing solar mass ejections, corotating regions, and shock waves through the heliosphere and forecast the arrival of heliospheric features at Earth in near real time. The HELIOS results provide the heritage for SMEI. SMEI represents an effective instrument architecture for near-Earth measurements. The labyrinthine-baffle design described here may be heavy for deployment to deep space. We have invented an alternative approach, appropriate when slightly more than a hemisphere free from illuminated obstructions can be made available on the spacecraft[33,37-40]. This technique views within several degrees of the Sun, much closer than the labyrinthine baffle described here, and is significantly lighter in weight. The SMEI concept has passed major milestones in design, prototype construction and test, and delivery of flight hardware for integration. We look forward to a successful launch and the onset of inflight data.

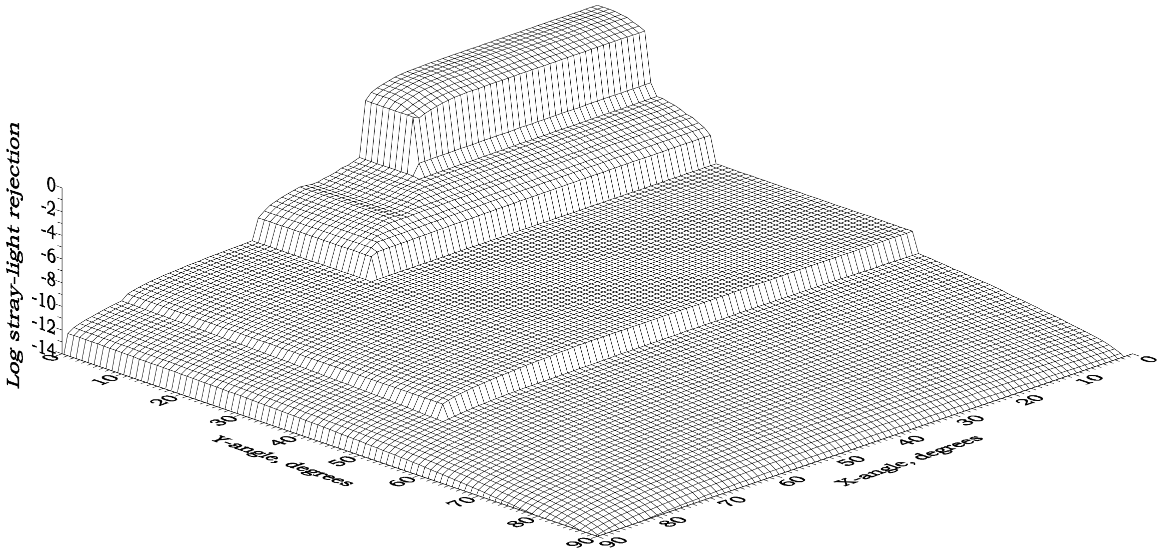

Figure 8. Plot of SMEI baffle stray-light rejection as a function of incident-light angles, normalized to unity at [0,0].

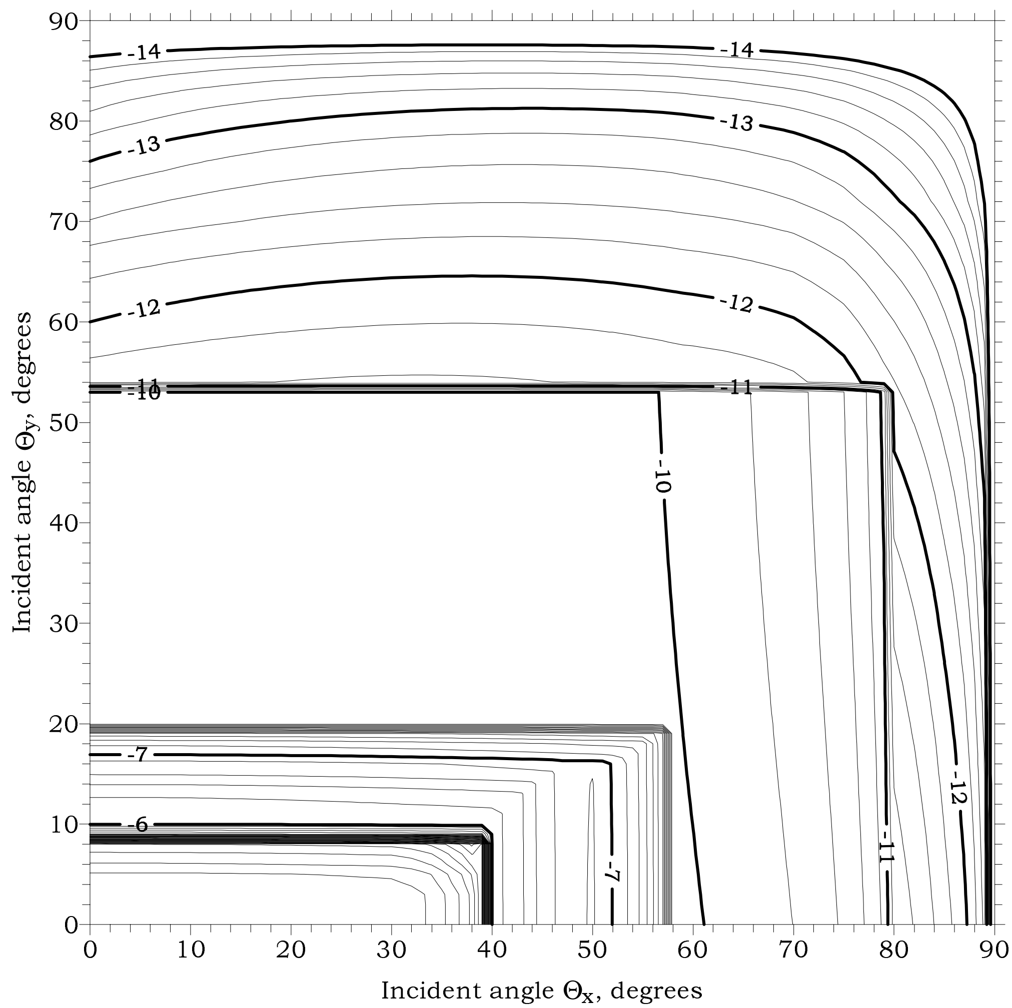

Figure 9. Same as figure 8, but a contour plot. Intervals here are 0.2 in $\log_{10}$ of baffle stray-light rejection.

ACKNOWLEDGEMENTS

The stray-light performance of the original WIND prototype baffle was measured at S. Koutchmy's laboratory at the Institut d'Astrophysique CNRS, Paris, France. We appreciate the interest and continuing support of R.C. Altrock. Initial design and evaluation of the WIND baffle, and the detailed APART calculations for the subsequent SMEI design, benefited much from the involvement of R.E. Gold and were supported in part by a subcontract to UCSD from U.S. Air Force contract F19628-87-0077 at the Johns Hopkins University Center for Applied Solar Physics. More recently, this work was supported in part by grant AFOSR-97-0070 and by subcontract F19628-00-C-0029 from the U.S. Air Force.

REFERENCES

1. C. Leinert, E. Pitz, H. Link, and N. Salm, "Calibration and in-flight performance of the zodiacal light experiment on HELIOS", *Space Sci. Instrum.* **5,** pp. 257-270, 1981.
2. B.V. Jackson and C. Leinert, "HELIOS images of solar mass ejections", *J. Geophys. Res.* **90,** pp. 10759-10769, 1985.
3. B.V. Jackson, "Imaging of coronal mass ejections", *Solar Phys.* **100,** pp. 563-575, 1985.
4. B.V. Jackson, R.A. Howard, N.R. Sheeley Jr., D.J. Michels, M.J. Koomen, and R.M.E. Illing, "HELIOS spacecraft and earth perspective observations of three looplike solar mass ejection transients", *J. Geophys. Res.* **90,** pp. 5075-5081, 1985.
5. D.F. Webb and B.V. Jackson, "The identification and characteristics of solar mass ejections observed in the heliosphere with the HELIOS-2 photometers", *ibid.* **95,** pp. 20641-20661, 1990.
6. B.V. Jackson, H.S. Hudson, J.D. Nichols, and R.E. Gold, "Design considerations for a 'solar mass ejection imager' on a rotating spacecraft", in *Solar System Plasma Physics*, J.H.Waite Jr., J.L. Burch, and R.L. Moore, eds., *Geophysical Monograph* **54,** pp. 291-297, 1989.
7. B. Jackson, R. Gold, and R. Altrock,, "The Solar Mass Ejection Imager", *Adv. Space Res.* **11,** pp. 377-381, 1991.
8. B.V. Jackson, D.F. Webb, R.C. Altrock, and R. Gold, "Considerations of a solar mass ejection imager in a low-earth orbit", *Eruptive Solar Flares*, Z. Svestka, B.V. Jackson, and M.E. Machado (eds.), Springer-Verlag, Heidelberg, pp. 322-328, 1992.
9. S.L. Keil, R.C. Altrock, S. Kahler, B.V. Jackson, A. Buffington, P.L. Hick, G.M. Simnett, C.J. Eyles, D. Webb, and P. Anderson, "The solar mass ejection imager (SMEI)", *Proc. SPIE* **2804,** pp. 78-89, 1996.
10. S.L. Keil, R.C. Altrock, S.W. Kahler, B.V. Jackson, A. Buffington, P.L. Hick, G. Simnett, C. Eyles, D.F. Webb, and P. Anderson, "The solar mass ejection imager (SMEI): development and use in space weather forecasting", in *Solar Drivers of Interplanetary and Terrestrial Disturbances*, K.S. Balasubramaniam, S.L. Keil, and R.N. Smartt eds., ASP Conference Series **95**, pp. 158-166, 1996.
11. B.V. Jackson, A. Buffington, P. Hick, S.W. Kahler, S.L. Keil, R.C. Altrock, G.M. Simnett, and D.F. Webb, "The solar mass ejection imager", *Phys. Chem. Earth* **22,** pp. 441-444, 1997.
12. D.F. Webb, J.C. Johnston, R.R. Radick, and the SMEI Team, "The solar mass ejection imager (SMEI): a new tool for space weather", *EOS, Trans. AGU* **83,** pp. 33, 38-39, 2002.
13. B.V. Jackson, "HELIOS spacecraft photometer observation of elongated corotating structures in the interplanetary medium", *J. Geophys. Res.* **96,** pp. 11307-11318, 1991.
14. B.V. Jackson and R.M. Benensöhn, "The HELIOS spacecraft zodiacal light photometers used for comet observations and views of the Comet West bow shock", *Earth, Moon Planets* **48,** pp. 139-163, 1990.
15. B.V. Jackson, A. Buffington, P.L. Hick, S.W. Kahler, and D.F. Webb, "A spaceborne near-earth asteroid detection system", *Astron. Astrophys. Suppl. Ser.* **108,** pp. 279-285, 1994.
16. B.V. Jackson, P.L. Hick, M. Kojima, and A. Yokobe, "Heliospheric tomography using interplanetary scintillation observations, 1. Combined Nagoya and Cambridge data", *J. Geophys. Res.* **103 (A6),** pp. 12049-12068, 1998.
17. M. Kojima, M. Tokumaru, H. Watanabe, A. Yokobe, K. Asai, B.V. Jackson and P.L. Hick, "Heliospheric tomography using interplanetary scintillation observations, 2. Latitude and heliocentric distance dependence of solar wind structure at 0.1-1 AU", *ibid.* **103 (A2)**, pp. 1981-1989, 1998.

18. K. Asai, M. Kojima, M. Tokumaru, A. Yokobe, B.V. Jackson, P.L. Hick and P.K. Manoharan, "Heliospheric tomography using interplanetary scintillation observations, 3. Correlation between speed and electron density fluctuations in the solar wind", *ibid.* **103 (A2)**, pp. 1991-2001, 1998.
19. P. Hick and B.V. Jackson, "Three-dimensional tomography of heliospheric features using Thomson-scattering data", *Proc. SPIE* **3442**, pp. 87-93, 1998.
20. B.V. Jackson and P. Hick, "Three dimensional tomography of heliospheric features using global Thomson scattering data", *Adv. Space Res.* **25**, pp. 1875-1878, 2000.
21. B.V. Jackson and P. Hick, "Time dependent tomography of heliospheric features using global Thomson-scattering data from the HELIOS spacecraft photometers during times of solar maximum", *EOS, Trans. AGU* **81,** S353 (abstract) 18-22 June 2000.
22. B.V. Jackson and P.P. Hick, "Real-time heliospheric forecasting – three-dimensional reconstruction of heliospheric features using remote-sensing data", the First S_RAMP Conference Abstracts, **96,** *SRAMP 2000*, Sapporo, Japan, 1-6 October 2000.
23. C.W. Allen, *Astrophysical Quantities*, 3rd edition, §73, §75 and §117, Athlone Press, London 1976.
24. A. Buffington, H.S. Hudson, and C.W. Booth, "A laboratory measurement of CCD photometric and dimensional stability", *Publ. Astron. Soc. Pacific* **102,** pp. 688-697, 1990.
25. A. Buffington, C.W. Booth, and H.S. Hudson, "Using image area to control CCD systematic errors in spaceborne photometric and astrometric time-series measurements", *ibid.* **103,** pp. 685-693, 1991.
26. R.P. Breault, "Problems and technologies in stray-light suppression," in *Stray-Light Problems in Optical Systems*, *Proc. SPIE* **107,** pp. 2-23, 1977.
27. R.P. Breault, "Vane structure design trade-off and performance analysis", *ibid.* **967,** pp. 90-117, 1988.
28. "Optical black coating", Martin Marietta Company, *ibid.* **107,** pp. 168-169, 1977.
29. S.M. Pompea and S.H.C.P. McCall, "Outline of selection processes for black baffle surfaces in optical systems", *ibid.* **1753**, pp. 92-104, 1992.
30. S.M. Pompea and R.P. Breault, "Black surfaces for optical systems,", chapter 37 in *Handbook of Optics, Volume II*, M. Bass editor in chief, McGraw-Hill, New York, 1995.
31. C. Leinert and D. Klüppelberg, "Stray light suppression in optical space experiments", *Appl. Opt.* **13,** pp. 556-564, 1974.
32. "ZEMAX®, optical design program," Focus Software Inc., PO Box 18228, Tucson, AZ 85731-8228, USA.
33. A. Buffington, B.V. Jackson and C.M. Korendyke, "Wide-angle stray-light reduction for a spaceborne optical hemispherical imager", *Applied Optics* **35,** pp. 6669-6673, 1996.
34. M. Born and E. Wolf, *Principles of Optics*, 6th ed. (Pergamon, New York, 1989).
35. K.A. Snail, D.P. Brown, J. Costantino, W.C. Shemano, C.W. Schmidt, W.F. Lynn, C.L. Seaman, and T.R. Knowles, "Optical Characterization of Black Appliqués", *Proc. SPIE* **2864**, pp. 465-474, 1996.
36. Breault Research Organization, "Arizona Paraxial Analysis of Radiation Transfer", 6400 East Grant Road, Suite 350, Tucson, AZ 85715-3862.
37. A. Buffington, P. Hick, B.V. Jackson and C.M. Korendyke, "Corrals, hubcaps and crystal balls: some new designs for very-wide angle visible-light heliospheric imagers", *Proc. SPIE* **3442**, pp. 77-86, 1998.
38. A. Buffington, "Improved design for stray-light reduction with a hemispherical imager", *Applied Optics* **39**, pp. 2683-2686, 2000.
39. A. Buffington, "Very-wide-angle optical systems suitable for space-borne photometric measurements", *ibid* **37**, pp. 4284-4293, 1998.
40. B.V. Jackson, A. Buffington and P.P. Hick, "A heliospheric imager for solar orbiter", Proc. of "Solar Encounter: The First Solar Orbiter Workshop", Puerto de la Cruz, Tenerife, Spain, 14-18 May 2001 (ESA SP-493, September 2001) pp. 251-256, 2001.

---

* abuffington@ucsd.edu; phone 858-534-6630; fax: 858-534-7051; http://casswww.ucsd.edu/solar/smei/index.html; mail code 0424, UCSD, 9500 Gilman Drive, La Jolla, CA 92093-0424

** bvjackson@ucsd.edu; phone 858-534-3358; fax: 858-534-2294

*** pphick@ucsd.edu; phone 858-534-8965; fax: 858-534-0177